Friedrich-Alexander-Universität
Faculty of Sciences

Bachelor's thesis

19-12-2025

Florian Foith

Shower based cross calibration of SWGO

Abstract

This work discusses the possibility of calibrating the effective efficiencies of Water Cherenkov detectors (WCDs) at the Southern Wide-field Gamma-ray Observatory (SWGO) by utilizing pairwise charge asymmetry parameters. These parameters are computed for single shower events and then averaged over all conducted simulations. The concept, originally proposed for Imaging Atmospheric Cherenkov Telescopes (IACTs), has proven successful for the Cherenkov Telescope Array (CTA) and is now being tested with two possible approaches for asymmetry parameter computation for SWGO. We found that following preliminary testing against grid anomalies, our method demonstrates promising accuracy within the limitations of WCD-based gamma-ray observatories.

Contents

1 Introduction

The study and investigation of gamma-ray or cosmic-ray induced air showers in Earth's atmosphere is a discipline of astroparticle physics and an observational method similar to radio- and visual astronomy. As a product of astronomical events like Supernovae, gamma- and cosmic-rays enter Earth's upper atmosphere where they produce air showers that can be detected indirectly either using pointing instruments like imaging atmospheric Cherenkov telescopes (IACTs) or on the ground using water Cherenkov detectors (WCDs) situated at high altitudes.

Water Cherenkov detectors are capable of surveying the entire sky for sources emitting high energy particles without significant interruption due to readjustments of the optics. This advantage allows scientists to survey not only the entire sky but also short-lived transient events like gamma-ray bursts. To produce useful contributions to scientific research, these observatories have to be precisely calibrated in order to recreate a detected event with a reasonable resolution. Only then is it possible to make a statement about the origin and also examine properties of the recorded shower to gain knowledge about its source.

So far, WCDs like the High Altitude Water Cherenkov Observatory (HAWC) and the Large High Altitude Air Shower Observatory (LHAASO) are built and operate in the northern hemisphere, with the southern sky being only observed via IACTs. The Southern Wide-field Gamma-ray Observatory (SWGO) is a WCD planned to be built in the Atacama desert to allow surveying the southern sky for gamma-ray and cosmic-ray events and to complement IACT observations with a focus on the galactic center.

The proposed SWGO project will consist of around 3700 individual tanks, which will each be separated in two chambers arranged above each other. This design is specifically created to optimize the separation between gamma and hadron induced air showers and is said to have superior discrimination abilities compared to existing projects like HAWC or LHAASO. To precisely calibrate a WCD, the efficiency parameter of every tank/chamber has to be determined. These depend on the installed Photo-Multiplier Tube (PMT), the water purity, and the water level inside the tank/chamber. Hence, a calibration technique is needed that addresses all possible effects.

The presented thesis will focus on the concept of cross-calibration using a χ^2-minimizer. The goal is to reach a satisfactory level of recovered efficiencies based on gamma-ray and cosmic-ray simulations. Fundamental properties of extensive air showers (EASs), the detection method of WCDs, and the design of SWGO will be discussed in order to explain the process of cross calibration based on shower simulations.

2 Fundamental topics and motivation

To understand the importance of calibration and the challenges that will be discussed later on, it is necessary to first discuss underlying physical concepts and technical methods. Therefore, an introduction and discussion of extensive air showers (EAS) will be made alongside an introduction to shower detection. A special focus will be put on the detection method utilizing the Water Cherenkov method and the designated method of SWGO using double layered detector tanks. Moving further, the SWGO project and its scientific goals will be introduced.
The description of air showers in section 2.1 is based on the work of J. Matthews and fully satisfactory for the purpose of this work since only the intuition and the concept of a shower event are needed to understand further elaborations [Matthews, 2005]

2.1 Properties of shower events

In general EASs, both hadronic and γ-ray showers, follow a similar structure of cascading particle production from an initial primary particle that entered the upper atmosphere. Since γ induced showers also occur as sub-showers for hadronic events and also have a simpler structure they will be introduced first. A realistic side by side comparison of simulations for a γ-shower and a proton-shower are portrayed in Figures 4 and 5.

A γ-shower is initialized by a γ-ray entering the upper atmosphere. After interaction with the electromagnetic field of an atmospheric molecule the γ-ray undergoes pair-production resulting in an electron-positron pair after traveling a fixed length given by

$$d = \ln(2)\ \lambda_{\mathrm{r}} \tag{1}$$

where λ_{r} is the radiation length of the medium the photon has passed. This process is the initial reaction of the shower cascade. The resulting particles propagate deeper into the atmosphere radiating energy by emitting photons via bremsstrahlung. These photons again undergo pair-production into another set of e^- e^+ forming the second step of the cascade. Here for simplicity reasons the reaction is only displayed for the relaxation of a single electron

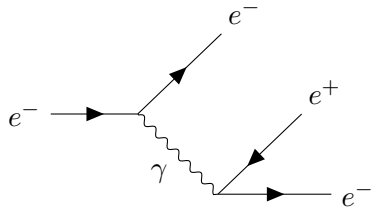

Figure 1: Feynman diagram of the second step in the γ-shower cascade.

This process happens until the particle energy is too low to initiate pair-production. The broadest lateral extension of the shower is reached when the energy of a shower particle falls below a critical energy where the reaction cross-section for scattering reactions is greater than the one for bremsstrahlung in case of electrons or pair production in case of photons. The loss of energy via scattering now dominates the probability of bremsstrahlung or pair-production. With further penetration into the atmosphere

the number of particles contributing to the shower decreases due to deflections from scattering reactions. As a result, the effective size of the shower and the number of its particles decreases. Hence the number of particles depends on the depth of the shower in the atmosphere. The number of particles in the shower after n cascade evolutions is approximated by $N = 2^n$ and the depth of the shower may be expressed as

$$D = n \cdot d = n \cdot \ln(2)\ \lambda_{\mathrm{r}}. \tag{2}$$

The critical energy depends on the density of the propagation medium. From that point forward the shower decreases in size again. For this reason, it is beneficial to operate WCDs at high altitude near the lateral shower maximum. However, installation and maintenance are increasingly difficult with higher altitudes.

For the case of hadronic shower events the production of particles is more complex than for γ-showers. The initial hadron which can vary from single protons to large nuclei like Iron will interact through the strong force with molecules of the upper atmosphere to produce both neutral and charged pairs of mesons like pions and kaons. Here we modify the expression defined in equation (1) to read

$$d = \ln(2)\ \lambda_{\mathrm{I}} \tag{3}$$

with λ_{I} denoting the interaction length for strong interactions. The length d now defines an atmospheric layer of interaction. The reaction releases a set of N_{ch} charged pions and $\frac{1}{2}N_{\mathrm{ch}}$ uncharged pions where the number of produced pions N_{ch} depends on the initial energy $E_0^{1/5}$ of the primary particle [Matthews, 2005]. From this step the π^0 propagates for a short time before it decays into a set of photons which themselves will introduce γ-sub-showers as described above.

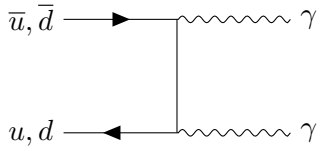

Figure 2: Feynman diagram of a π^0 decay

The $\pi^{\pm}$ propagates onward into the next layer d where it may again interact strongly to produce similar reaction products. In that manner a new set of π^0 induced γ-sub-showers is introduced to the hadron shower while the produced $\pi^{\pm}$ interact again. In each evolution a third of the initial proton or later $\pi^{\pm}$ energy is released into the γ-sub-shower meaning that the produced charged pions yield an energy of $\frac{2}{3}E_{\mathrm{i}}$ where E_{i} is the initial energy of the proton or pion prior to the interaction. Typically with each step of the cascade multiple pions are produced each pion has significantly less energy than its predecessor particle. Similar to the γ-ray the charged pion will reach a critical energy where the decay into muons dominates.

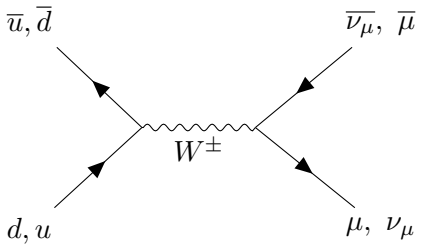

Figure 3: Feynman diagram of a weak pion decay through a W-boson whereas a π^+ decays into a $\overline{\mu}$ and a ν_μ and a π^- into a $\overline{\nu_\mu}$ and a μ

Since muons are primarily produced in hadronic air showers they will therefore also be used to differ a detected shower between γ or hadron induced. A detailed analysis of this discrimination is provided in chapter 2.3. Similar to the γ-shower the hadronic shower reaches its lateral maximum at the depth of maximum lateral expansion of the γ-sub-showers.

The introduced model of EASs describes the origin of an air shower and its propagation towards the detector and Earth's surface. A more detailed description of EASs is surely possible to derive but not necessary for the purpose of this work so this work will stick to the simplified model.

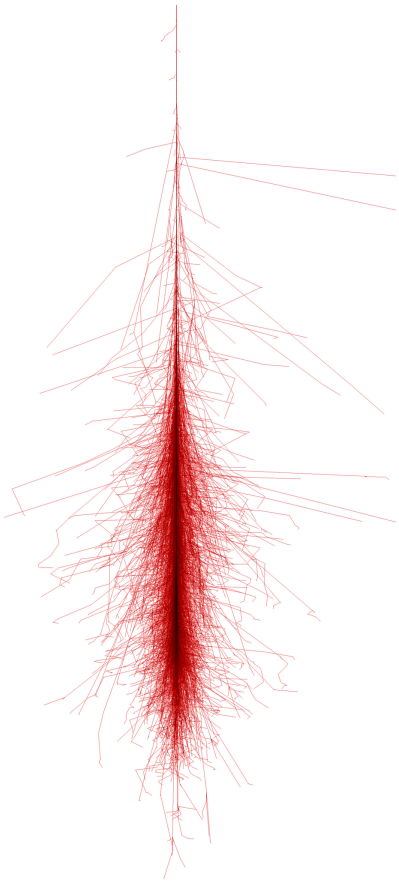

Figure 4: CORSIKA simulation of a 100 GeV gamma shower entering earths atmosphere [DESY, 2025a].

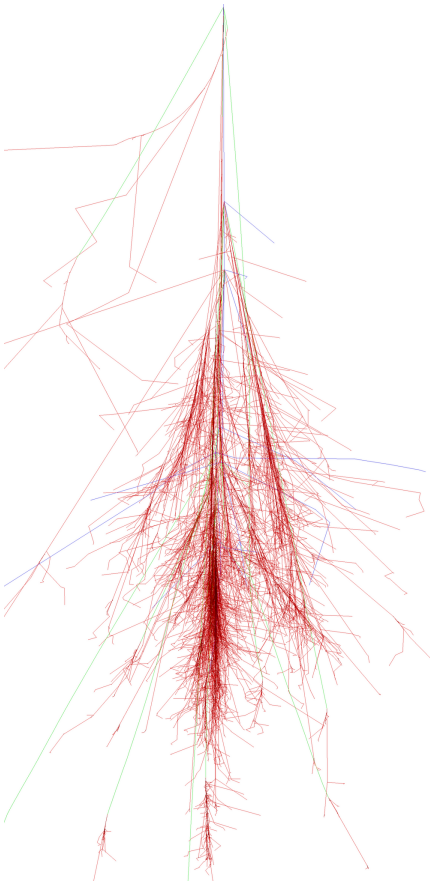

Figure 5: CORSIKA simulation of a 100 GeV proton shower entering earths atmosphere [DESY, 2025b].

2.2 CORSIKA Simulations

This work will use shower simulations created with the CORSIKA event simulation tool developed by the Karlsruhe-Institute of Technology (KIT) [D. Heck, 1998]. CORSIKA is a software that simulates cascades of particle production in the atmosphere and therefore is mainly used in astroparticle physics to simulate shower events. CORSIKA allows the simulation of shower events under universal assumptions regarding important physical models of particle interaction.
The event cascades of this work are a set of Monte Carlo simulations created with CORSIKA used for the D8 layout of the SWGO array as discussed in [SWGO-Collaboration et al., 2025]. The actual dataset is labeled M7 internally since it was simulated in progress of Milestone 7 of the SWGO project (see figure 6 for the milestones). The PMT response is simulated using HAWCsim and evaluated using AERIE, which are software tools originally developed for HAWC [HAWC, 2025]. Two or more events triggering the array are possible but not discussed for the current simulation setup.

2.3 Discussion of the Water Cherenkov detection method

This subsection will introduce the water Cherenkov detection technique that will be used for SWGO and also explain the designated setup using double layered water tanks. In general an EAS is detected via secondary photons by shower particles. In the past, detection was traditionally carried out using a scintillator to count event particles. This was proven ineffective for γ-shower events due to a very low sensitivity of a scintillator array with only 1-2 % while yielding an energy threshold of around 100 TeV [Sinnis, 2010]. A further approach of detection was made using a water tank to detect Cherenkov light. The underlying principle of this detection method is the Cherenkov effect. It describes a phenomenon of light emission when a particle moves faster than the local speed of light. Cherenkov light is emitted by the medium if charged particles travel faster than the local speed of light. The first proof of this concept was made by the Milagro project which was capable of detecting multiple low TeV sources [Sinnis, 2010]. The general theory states that for a particle with a speed $v < c$ where c is the vacuum speed of light Cherenkov light can be produced when the relation

$$\frac{v}{c} = \beta > \frac{1}{n} \qquad \text{with } n \text{ as the refractive index} \tag{4}$$

is satisfied. In that case the particle that entered the medium moves faster than the local speed of light c_{local} which also can be derived from the refractive index. For pure water the local speed of light is given as $c_{\text{local}} \approx 0.75c$. The Cherenkov effect can be simplified as a shock front formed by the moving particle similar to a supersonic shock wave. The Cherenkov shock is detected as a light cone of UV- or visible blue light, depending on the medium. The Cherenkov angle describes the angle enclosed by the propagation direction of the particle and a normal vector placed onto the shock front and is defined as

$$\cos \theta_{\text{Ch}} = \frac{1}{\beta n}. \tag{5}$$

Depending on the size of the WCD tank, multiple photomultiplier tubes (PMTs) are used to reconstruct the detected Cherenkov light or, as proposed in the wide-field γ-ray observatories such as SWGO, Cherenkov light is detected with only a single PMT. Hence, certain dimension ratios as well as reflectivity abilities of the inner tank walls are required. The following design details are based on the SWGO white-paper, which outlines the current status of the project and discusses the considered tank dimensions [SWGO-Collaboration et al., 2025].

The currently designated design features tanks with a radius of 5.2 m and a height of 4 m. Inside there will be two chambers to optimize γ/hadron separation and the lower chamber will have a height of 80 cm. The upper chamber is set to host a 10 inch PMT and the lower chamber will host an 8- to 10-inch PMT which is still to be decided. Furthermore, the lower chamber will have a highly reflective lining at the top end of the chamber to improve the detection of Cherenkov light.

2.4 Analysis and reconstruction of shower events

A detected air shower allows the deduction of information about its source; hence, parameters like age or activity may be examined. The intensity of a shower indicates the physics of the initial particle acceleration and therefore carries information about properties of its source. To reconstruct shower parameters, the zenith angle, shower core, azimuth angle and shower energy must be determined. While the energy can be reconstructed from the total photoelectron yield in the PMTs, information about the impact location and angles is usually derived from timing information between the tanks. From the detection time of each tank the shower front can be reconstructed and together with the information about the recovered integrated PMT charge in any tank the impact location and angles can be recovered [Abeysekara et al., 2017]. A different approach to reconstruct the core and energy is proposed by [Abreu et al., 2023] which is only dependent on the recovered charge in each tank. The technique has been originally developed for the High Altitude Water Cherenkov array (HAWC) and was adapted for SWGO. It has been proven to reconstruct events based on Monte Carlo simulations. The main idea of the approach is to consider the charges recovered in each tank and create an amplitude function for the event. For this function using Monte Carlo (MC) simulations and HAWCSim a probability distribution function is computed for each tank and fitted against the observed amplitude function. From the best fit one can retrace parameters like zenith angle, shower impact location, etc. and therefore reconstruct the recorded event.

2.5 The proposed SWGO project

The SWGO is a project that aims to investigate very high energy (VHE) γ-ray events originating in the southern hemisphere. The project will be summarized along the lines of the SWGO white paper [SWGO-Collaboration et al., 2025]. Once fully operational, the wide field capability of SWGO allows for a continuous monitoring of the galactic plane to observe and study particle acceleration and the galactic structure. Figure 8 displays the accessible regions of the sky also highlighting the extension of the observable sky by collaborating with *Fermi*-LAT. The high energy detection capability and large Field of View (FoV) combined enable the detection of transient events like Gamma Ray Bursts (GRB)s, flares from active galactic nuclei (AGN flares) and Nova or Supernova explosions. Further proposals regarding beyond Standard Model physics are also under discussion, namely detection of dark matter (DM) annihilation or decay which in theory would also create VHE or ultra high energy (UHE) γ-ray detectable for SWGO.
A further notable extension is the *The Utility for Radio Beam-formed Observations* (SWGO-TURBO) project which will enhance angular resolution and shower characteristics for large zenith angles.
The designated site *Pampa La Bola* in the Atacama Astronomical Park lies at 4.7 km above sea level and is located 45 minutes of driving away from the town San Pedro de Atacama. This site is a well established location for astrophysical observatories also hosting the Large Millimeter/submilimeter Array (ALMA) for example. The altitude is a dominant factor since it allows the indirect detection of secondary shower particles in water tanks as explained in section 2.3. The project is still in development nearing the first construction phase [SWGO-Collaboration et al., 2025]. The project is categorized in milestones with the latest achieved milestone M7 being the decision for the project

site. All defined milestones can be retraced in Figure 6 and show that the project is nearing its operational status with construction beginning after the design is finalized.

	Milestone	Completed
M1	R&D Phase Plan Established	Q1 2020
M2	Science Benchmarks Defined	Q2 2020
M3	Reference Configuration & Options Defined	Q4 2020
M4	Site Shortlist Complete	Q3 2022
M5	Candidate Configurations Defined	Q1 2022
M6	Performance of Candidate Configurations Evaluated	Q3 2023
M7	Preferred Site Identified	Q2 2024
M8	Design Finalised	-
M9	Construction & Operation Proposal Complete	-

Figure 6: Table of Milestones taken from [SWGO-Collaboration et al., 2025]

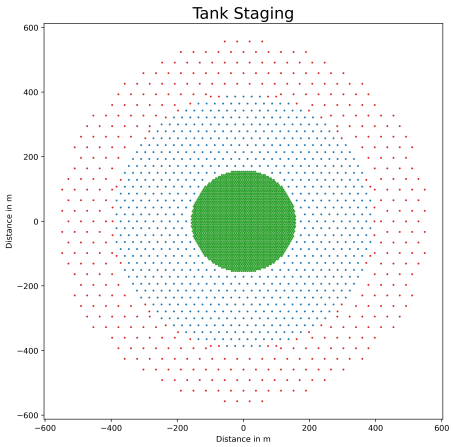

Figure 7: Plot of the M7 tank layout.

With the current status of the project, a tank layout as seen in Figure 7 consisting of 3 stages with a total of 3763 WCDs. The stages differ mainly in terms of fill factor with the center-most stage yielding 70% the middle stage 4% and the belt stage 1.7%. The high fill factor in the center is necessary to allow for transient and distant source detection while the low fill factor and therefore larger ground area covered by the two outer stages allow a higher rate of PeV shower detections. With this setup the entire array will cover 1 km^2 on the ground. The tank design for the center stage follows the principle explained in section 2.3. The double layered design features superior capabilities in terms of γ/hadron separation when compared to single chamber tanks used for the HAWC array [Kunwar et al., 2023]. The WCD units consist of steel tanks with a bladder incorporated to hold the water and PMTs. These tanks are set with a radius of 5.2 m and height of 4.1 m whereas the bladder has a total hight of 4 m and depth of 3.2 m for the upper chamber. The used PMTs are still under discussion but for the upper chamber a 10-inch PMT is favored whereas for the lower chamber an 8- to 10-inch PMT is said to be reasonable.
For the two outer array stages the final tank design has not been determined due to ongoing discussions about dimensions and chamber layouts. A similar design as used in the center is possible yet different designs with financial and logistic benefits are still plausible. Possible alternative options contain a smaller tank design which may be built on site but lack the superior γ/hadron separation ability [SWGO-Collaboration et al., 2025]. A first feasibility test of possible tank designs will be conducted under the project name SWGO-*Pathfinder* (SWGO-PF) consisting of six tanks of different setups to investigate the individual response under real conditions on site. After completion of the SWGO-PF test SWGO-A will be constructed in close proximity and begin observations with a fraction of the center stage tanks. SWGO-A will consist of 385 WCDs grouped in 7 clusters with a central Field-node (FN) for power supply and data recovery and a grid fill factor of 65%.

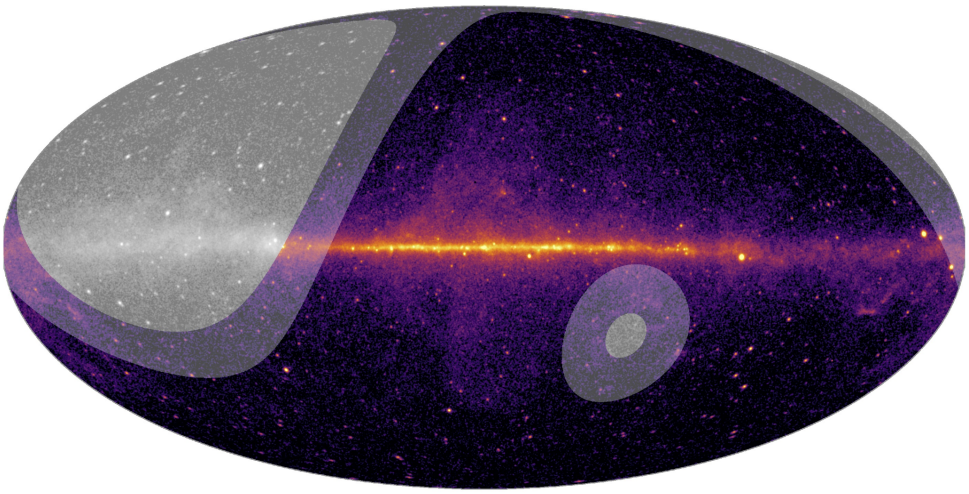

Figure 8: SWGO FoV taken from [SWGO-Collaboration et al., 2025]. Colored area shows direct FoV,the dimmed area the combined area with *Fermi*-LAT and gray area the SWGO blind spot.

3 Calibration process

The basis for a proper operation of the array is the identification of the tanks' efficiency parameters. This calibration is crucial for scientific usability and can be conducted in many different ways. The simplest approach is to use a laser or a different light source of known energy and illuminate the tank from above. From the detected number of photoelectrons in the PMT an efficiency factor for the tank can be computed, which is contributed to by the PMTs' efficiency, the purity of the water, which has a great influence on the radiation length of entering particles and photons, and the water level within the chamber. In contrast, this thesis aims to test a cross-calibration of all tanks. The principle is derived from the work of [Mitchell et al., 2016] building on the fundamental work of [Hofmann, 2003]. Cross-calibration allows the recovery of effective efficiency parameters of all tanks based on Monte Carlo simulations of EASs. The efficiencies will be recovered as minimization fit parameters to a set of asymmetry parameters of pairwise comparisons between tanks. For the purpose of this work, the simulation set D8/M7 of CORSIKA simulations was used. For CTA, the accuracy of the recovered efficiencies was mostly constrained within 5% of the initially assigned dummy efficiencies, based on ≈ 40000 eligible events [Mitchell et al., 2016].

3.1 Mathematical foundation

The goal of the minimization as described by [Hofmann, 2003] is to find a set of parameters c_i for a set of i tanks to minimize the equation

$$s_{ij} := \frac{S_i - S_j}{S_i + S_j} \approx \frac{c_i - c_j}{c_i + c_j} \tag{6}$$

whereas S_i defines the detected PMT charge in each tank. s_{ij} denotes the size asymmetry parameter for the tank pair t_i, t_j and defines the measured charge asymmetry between

two tanks. To recover only reasonable asymmetries for a given tank i, a proximity has to be set for each of the grid zones (center, middle, belt) to make sure a reasonable amount of asymmetries is found, but also the number of considered tanks will not exceed a certain range from the considered tank i. Otherwise the shower geometry will vary too much and the size asymmetry is not useful. For the found set of tank pairs, the size asymmetry is calculated and introduced to the minimizer to find a set of efficiency parameters. The minimizer is defined as

$$\chi^2 = \sum_{i,j\neq i} \frac{(s_{ij} - \frac{c_i - c_j}{c_i + c_j})^2}{\sigma_{ij}^2}. \tag{7}$$

This χ^2-minimizer sums over all found index pairs $(i,\ j)$ where $i \neq j$ must hold since otherwise s_{ij} is trivial and the minimizer will not work for this pair. The key attribute of this minimizer is the weighting of the minimization by σ_{ij} defined as

$$\sigma_{ij} := 2 \cdot \frac{\sqrt{S_j^2 \cdot \sigma_i^2 + S_i^2 \cdot \sigma_j^2}}{(S_i + S_j)^2} \qquad \text{with} : \sigma_i := S_i \cdot 0.04. \tag{8}$$

The factor of 0.04 is a logarithmic factor added in the progress of event simulation and represents the recorded PMT noise. To calculate the standard deviation σ_{ij} for the asymmetry parameter s_{ij}, the assumption that both S_i and S_j are measured independent from each other is made together with the fact that each have a measurement uncertainty of Ω which leads to

$$\sigma_{i,j} := S_{i,j} \cdot \Omega. \tag{9}$$

Now σ_{ij} is understood as the propagation of uncertainty as

$$\sigma_{ij} = \sqrt{\left(\frac{\partial s_{ij}}{\partial S_i}\right)^2 \sigma_i^2 + \left(\frac{\partial s_{ij}}{\partial S_j}\right)^2 \sigma_j^2}. \tag{10}$$

First by calculating the derivations with respect to $s_{i,j}$ the equation is simplified.

$$\frac{\partial S_{ij}}{\partial S_i} = \frac{\partial}{\partial S_i} \cdot \frac{S_i - S_j}{S_i + S_j} = \frac{2S_j}{(S_i + S_j)^2} \quad \text{and similar} \quad \frac{\partial S_{ij}}{\partial S_j} = \frac{2S_i}{(S_i + S_j)^2} \tag{11}$$

Those are inserted into the equation and after further simplifications one finds

$$\sigma_{ij} = 2\frac{\sqrt{S_j^2 \cdot \sigma_i^2 + S_i^2 \cdot \sigma_j^2}}{(S_i + S_j)^2}. \tag{12}$$

σ_{ij} is referred to as the weighted standard deviation because additional weight is assigned to pairs with tanks that show a differing response and can thereby be calibrated efficiently. It's evident that when a tank pair approaches $S_i \approx S_j$ that σ_{ij} will grow and when $S_i << S_j$, σ_{ij} will decrease. In the case of $S_i \approx S_j$ one can identify the uncertainties and charges of S_j with S_i

$$\sigma_{ij} = 2\frac{\sqrt{S_j^2 \cdot \sigma_i^2 + S_i^2 \cdot \sigma_j^2}}{(S_i + S_j)^2} = 2\frac{\sqrt{S_i^2 \cdot \sigma_i^2 + S_i^2 \cdot \sigma_i^2}}{(S_i + S_i)^2} = 2\frac{\sqrt{2(S_i \cdot \sigma_i)^2}}{(2S_i)^2} \tag{13}$$

when inserting the given expression σ_i reads

$$\sigma_{ij} = 2\frac{\sqrt{2 \cdot \Omega^2 \cdot S_i^4}}{(2S_i)^2} = \frac{\sqrt{2}}{2} \cdot \Omega = \frac{\Omega}{\sqrt{2}}. \tag{14}$$

When the approximation of $S_i << S_j$ is made, to compute the equation one first has to evaluate the denominator. Then the substitution $S_i = \alpha S_j$ is introduced and the assumption $S_i << S_j$ implemented by setting $\alpha \mapsto 0$. Doing so results in

$$\sigma_{ij} = \frac{\sqrt{S_j^2 S_i^2 \Omega^2 + S_j^2 S_i^2 \Omega^2}}{(S_i + S_j)^2} \overset{S_i = \alpha S_j}{=} \frac{\sqrt{2\alpha^2 \Omega^2 S_j^4}}{S_j^2(1+\alpha)} = \frac{\sqrt{2}\alpha\Omega}{1+\alpha} \tag{15}$$

for $\alpha \mapsto 0$ one finds $\sigma ij \overset{\alpha \mapsto 0}{\longrightarrow} 0$. This way σ_{ij} leads to the relative weighting of tanks pairs with a high asymmetry and therefore a greater contribution to the minimizer. The reason for this is that the asymmetry of tanks with similar charge converges to 0, leading to trivial c_i/c_j recoveries, whereas differing sizes $S_{i,j}$ yield a large asymmetry which is ideal for calibration purposes.

3.2 Theoretical approach

Before the implementation of the mathematical concept can be made, one first must think of an efficient theoretical structure upon which the minimizer will be applied. These considerations need to respect both technical and practical viewpoints that will be discussed in this section alongside a brief explanation of the tests that will be run for the SWGO layout.

As first priority, the benchmarks for the calibration have to be determined.
Since the planned layout will consist of three clearly differing stages, it makes sense to calibrate these stages individually. When an event strikes the array, it is intuitive that the asymmetry of two tanks in the center array, which has a high fill factor and therefore only a small tank separation will on average show a smaller difference than a measured asymmetry in the outermost belt section with a very small fill factor and large separation distances. Hence, the first step will be to evaluate the minimization in 3 separate zones, them being the center, middle and belt stages. For these three sets the average distance between the tanks of a pair is comparable within the stage and therefore the main difference between two tanks is governed by the lateral intensity profile of the shower and the efficiency of each tank. Later, two approaches will be introduced with the goal to create a set of asymmetries for tank pairs gathered from multiple simulation events that were evaluated under strict quality cuts.

Core r [m]	Zenith θ [°]	Hits [N]	Chamber
$r \leq 700$ m	$\theta \leq 20°$	$60 \leq N$	upper/lower

Table 1: Quality cuts enforced on simulation events

The cuts are set to discriminate the full set of shower simulations ($\approx 3.6 \times 10^6$ events) to select only those events which allow for good efficiency calibration. The cuts will mask

for showers that are fully or mainly contained within the array by setting a maximum radial distance for a core impact from the array center. Since the used array layout has a radius of ≈ 560 m the radial cut for shower cores is set to 700 m. To rule out the possibility of shadowing effect in the center stage for now a zenith angle of less then $20°$ is enforced. Beside the core cut and the zenith angle the most dominant attribute is the shower energy since the calibration of events close to the array threshold would not be beneficial to the calibration. The simplest way to rule out low energy events would be by energy discrimination but here a cut on the number of triggered tanks was chosen. This indirectly masks out showers with low energy and also prevents events governed by noise signal to enter computations. Furthermore, simulations of events with fewer corresponding hits won't be considered by SWGO. Since calibration is split for each chamber the masked events will be distinguished by chambers as well so that after the cuts an event entering the staging process and later calibration only consists of hits in a designated chamber. In Table 1 all enforced cuts can be traced.

With respect to the discussed cuts, the calibration process can now be defined. In the following, the original approach of [Mitchell et al., 2016] will be explained with reference to mathematical structures as worked out in section 3.1 and adaptions for SWGO will be highlighted. Additionally, a second approach using a different workflow and minor but efficient changes in the computation of asymmetry parameters will be presented. A third potential option will only be briefly mentioned without explicit implementation.

Asymmetry averaging The CTA approach will also be referred to as *asymmetry averaging approach* in the following. For CTA each telescope i is assigned a global efficiency parameter g_i containing efficiency influencing factors like the reflectivity of the telescopes mirrors and the readout efficiency of the camera sensor. The approach acquires asymmetries by detecting events under quality cuts regarding shower containment in the grid, zenith angle, etc. The calculation of asymmetries was made for events triggering at least two telescopes. Within the set of active telescopes in a detected event, for each telescope a proximity distance was set in which eligible telescopes have to be situated in order to allow asymmetry calculations. This requirement ensures that the detectable charges the telescopes i and j of a designated pair may recover are comparable. For each triggered telescope, all asymmetries within the proximity are computed and will be saved for the given index pair. This process is repeated for N events and afterwards the resulting list of asymmetries for a pair (i, j) is averaged to display the designated pair asymmetry. That way, one set of averaged asymmetries with only one asymmetry per pair is computed, which will then be minimized as explained in section 3.1. The averaging reduces the negative effect that can occur for single events when the charge difference between two neighboring tanks is very high due to the shower geometry. Single events creating large asymmetries between two tanks will not have a big influence in the averaged asymmetries resulting in fairly moderate set of asymmetries that will be handed to the minimizer. The quality of the minimizer is determined by subtracting the minimized set of c_i from the dummy efficiencies g_i assigned to the telescopes at the start. The calibration will find 0% offset in case of perfect minimization. The studies found that the parameters c_i can be recovered with an accuracy mostly contained within 5% of the actual parameters. This level of quality was achieved after evaluation of 35 million

simulations containing roughly 40000 events eligible for asymmetry calibration. The study confirmed the principle established by [Hofmann, 2003] for IACTs. In this thesis the adaption of this approach will be tested for ground-based gamma-ray observatories like SWGO. Figure 9 highlights the important checkpoints for this calibration approach.

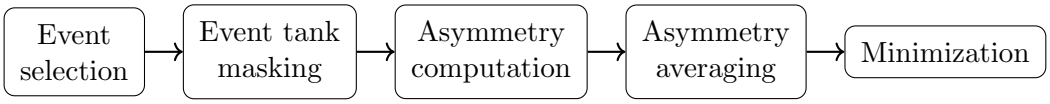

Figure 9: Workflow for asymmetry averaging approach

Charge averaging The *charge averaging approach* follows the same concept and was deduced from the CTA version for the sake of this work. The main goal of this approach is to resolve a lack of accuracy that is systematically inherited in the asymmetry averaging approach. The charge averaging also leads to a simplification of the calibration process. This simplification is achieved by averaging the detected charge per tank over all triggered events rather than averaging the asymmetry for a tank pair. By summing the detected charge per tank i for a set of N simulations and averaging for each tank depending on the number of detected events the grid will converge towards an even illumination of all tanks. The assumption is that the detectable charge for each tank can be approximated as a Gaussian distribution peaking at an arbitrary charge. For N events the charge a triggered tank records will fluctuate around the arbitrary peak. When $N \mapsto \infty$ or a considerably high number of events the total charge a single tank records will converge towards $N \cdot Q_{\text{peak}}$ where Q_{peak} is the charge at the Gaussian peak. Since this is the same scenario for every tank, the main contribution to charge differences and therefore the main dependency of the asymmetry is set by the tank efficiencies. For charge averaged tanks only one set of asymmetries is computed since the summation of N events can be interpreted as a single event. This way an optimized set of asymmetries is introduced to the minimizer leading to high accuracy recoveries. It is very important to note that the required statistics in terms of events may exceed the required statistics for the CTA like approach by some orders of events because of the requirement of very even illumination.

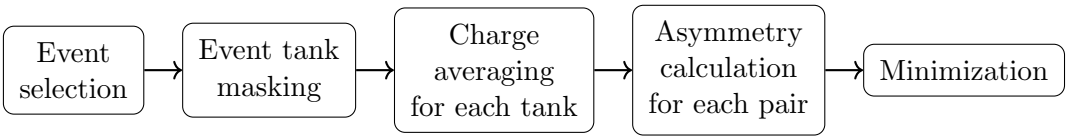

Figure 10: Workflow for charge averaging approach

The third mentioned approach is comparable to the asymmetry averaging approach but with an exception that might lead to a higher recovery quality. This approach also aims to average pairwise asymmetries similar to the CTA version but with the addition that asymmetries are only computed in equidistant rings around the shower core. That way it is ensured that tanks that are compared already yield comparable charge resulting in moderate asymmetry values leading to a more precise recovery than with the asymmetry averaging as discussed before. Regards to the feasibility and possible problems during

the implementations are briefly discussed in section 5.

3.3 Implementation

The implementation is built in a modularized structure of six main functions. Both addressed approaches make use of these with slight transformations for the given approach. A brief overview of the code operations is on display in Table 2. The basic structure of the implementation will be explained, which realizes event selection and discrimination with respect to quality cuts. They realize the event selection and discrimination with respect to quality cuts. Further, the separation of triggered tanks from inactive tanks as well as the setup of the data structure and processes of stage distribution and asymmetry calculation are implemented. Unique code sections of each approach will be explained in the process. Comments towards identified potential for optimization of code elements will be made in section 5. As a notable comment the entire implementation is done in *Python* and can be run on a standard PC or Laptop. With the used setups (2024 Apple M3 CPU or AMD Ryzen 5 5600G) the entire calibration only takes a few hours to compute. The implementation can be found on the corresponding ECAP repository [Foith, 2025].

Function	Execution duty
`main()`	Event selection based on set cuts. Events are handed over to `mask()`. Later receives results from `mask()` and saves them for evaluation.
`mask()`	Separates triggered from inactive tanks and initializes data structure. Communication with `asym()` and later with `calibrate()`. Hands calibration results back to `main()`.
`asym()`	Receives simulation data from `mask()` and organizes tanks in center, middle and belt stage. Forwards data to `compute()` for asymmetries calculation. Hands computed asymmetries back to `mask()` already structured for `calibrate()`.
`compute()`	Computes asymmetries and sets structure for `calibrate()`. Hands evaluated tanks back to `asym()`.
`calibrate()`	Evaluation of tank calibration based on calibration requirements. Communication with `chi()` during minimization. Hands calibration results back to `mask()`.
`chi()`	Addressed during minimization to form χ^2 expression and σ_{ij} values.

Table 2: Communication structure of all functions. This structure is global and changes between approaches lie within each function

3.3.1 Workflow

The process is started when a set of simulation files was loaded into the code and each file contains multiple Monte-Carlo simulations. After a desired number of files was loaded into the code the `main()` function will start a loop over all detected events within those files and select events based on the cuts from Table 1. The simulation files

used here are structured in *fields* as portrayed in section A.1.1. The loop runs over the total number of hits for an event. For each event the loop recreates the shower core to compare it to the core cut alongside with the zenith angle cut. Events passing the test will then be investigated for minimum number of hits in the designated chamber. After these cuts the PMT locations along with the PMT charge are stored in a list for later use. Furthermore, a small loop is run to apply tank efficiencies and assign the dummy efficiency that is set to be recovered at the end. Figure 11 shows a simplified version of this loop. The assigned dummy efficiencies follow a Gaussian distribution centered around 100% efficiency with a standard deviation of 15%. Afterwards, a set of event data lists will then be handed forward to the `mask()` function. After the computations in `mask()`, the results will be ultimately handed back to `mask()`, where they will be processed and saved. With the next step, the `mask()` function will receive the lists

```
>loop over events:
    >Counter = 0
    >showercore = ....
    >Zenith angle = .....
    >if Zenith cut is passed and Corecut is passed:
        >loop over tanks:
            >if tank chamber passed:
                >Counter += 1
        >if Counter passes cut:
            >Event is recognized and Data is saved in lists:
             X_position_list, Y_position_list, Charge_list,
             Core_list, TankID_list, ChamberID_list,
             Efficiency_list
```

Figure 11: Abstract version of `main()` loop to qualify events for calibration

created in `main()` and loop them again with the goal of computing the effective charge in each tank by multiplying the charge with the tank efficiency. The `mask()` loop will only check the tank chamber and then address each tank and its data. Here the code starts to differ for the chosen approach.

Charge averaging approach For the charge averaging approach, the position, charge, efficiency and index of each tank will be collected. When a tank is triggered by an event the effective recorded charge is calculated and then saved (see Figure 12). For each tank this process is repeated for each event and after the loop is complete the charge of each tank is averaged from all recorded charges of this tank. With the resulting data sets the `asym()` function will be called. The results from `asym()` are then handed to `calibrate()` separated for center, middle and belt stage to perform minimization and those results are received and handed back to `main()`.

Asymmetry averaging approach For the asymmetry averaging, the initial call for `mask()` stays the same as for the charge averaging, with the only exception that `asym()` is called for every iteration of the event-loop. That way, each event will have

```
>create lists for position, charge, efficiency and index here
 with sublist for each tank
>loop over events:
    >loop over tanks:
        >if chamber cut approves:
            >effective_charge = charge * efficiency
            >save: tank position, effective_charge, efficiency
             and index to tanklist
>average effective_charge for each tank over number of events
>call asym()
>hand results back to main()
```

Figure 12: Abstract structure of important `mask()` features

its own set of pairwise asymmetries, which will be saved. The averaging will be done in `calibrate()`.

For simplicity reasons, `asym()` was structured in a way that both approaches can make use of the same block. For the charge averaging, `asym()` receives a data structure of multiple events that have been transformed to portray a single very large event, and for the asymmetry averaging, each event inheriting the same data structure is passed to `asym()`. `asym()` will then start a distribution-loop to sort the tanks and their data into the array stages, which will be used in the asymmetry loop. This will run over all tanks of a stage and enter `compute()` for each iteration. In `compute()` the initial tank is fixed and a loop over the remaining tanks is started to check for tanks in a defined proximity around the initial tank. For a selected tank, the asymmetry parameter is then computed and saved for this pair, along with both tank charges. This structure is later needed in `calibrate()` to ensure correct minimization and for the correct averaging of asymmetries. After finalizing the results for each tank, the pairwise asymmetries are handed back to `mask()` where they will be transferred to `calibrate()`. The basic structure of `asym()` and compute can be seen in Figure 13.

```
----------------------------asym()-----------------------------------
>loop over tanks:
    >calculate distance to array center
    >distribute in array stages
>loop over tanks in center/middle/belt stage:
    >for tank i start compute()
    >save set of pairs received from compute() for mask()
>hand set of stage and tankwise asymmetry pairs to mask()

---------------------------calibrate()-------------------------------
>for fixed i, loop over all tanks j:
    >if tank j is in stage explicit proximity to i:
        >compute asymmetry
        >save data: (asymmetry, (index_i, index_j), charge_i, charge_j)
>hand set of pairwise asymmetries back to asym()
```

Figure 13: Workflow structure of `asym()` and `compute()`

In `calibrate()`, the minimization requires the actual χ^2 formula, which will be computed in `chi()`.

Charge averaging approach Here, `calibrate()` will receive a set of pair asymmetries structured by `compute()` as described in Figure 13. The first step is to determine if enough asymmetries have been computed to allow calibration. If a nonzero number of pairs was found, the frequency of the index i (i, j) of each asymmetry will be determined to determine the total amount of asymmetries a tank i has initialized. The tanks entering the calibration are constrained to only host eligible tanks with at least 3 initialized asymmetries. As a second fail condition, the minimum number of 2 eligible tanks is checked, because with only one eligible tank, a calibration is not possible. When this condition is passed, a reference tank is chosen for scaling reasons of the minimizer. The reference tank is set to be the strongest tank, so the tank with the most asymmetries. If many tanks have equal amount of asymmetries, the reference is chosen arbitrarily. The set of asymmetries, indices, and tank energies is now minimized. The minimizer therefore calls `chi()` to calibrate the recovery efficiencies. Figure 14 sketches the main structure.

Asymmetry averaging approach For the asymmetry averaging, the structure stays the same with the addition of the averaging, which is conducted as the first step in `calibrate()`. The set of event-wise asymmetries from `mask()` will now be separated for each contributing pair of the tanks i and j. For each pair, the charges of both tanks will then be averaged over all triggered events as well as the asymmetry, which will be averaged in similar fashion. Then `calibrate()` will operate in the same structure as for the charge averaging approach.

The final part is the `chi()` function, which will be called very frequently since the

```
-----------------asymmetry averaging add on-----------------------
>loop over all events:
    >loop over asymmetries in event:
        >sort pairs into global set of pair specific asymmetries
>average tank charge of pair tanks
 and pair asymmetry over all events triggered

----------------similar strucutre from here on---------------------
>check number of pairs
>if no pairs found:
    >no calibration -> break
>count number of pairs initialized by each tank
>qualify strong tanks with at least 3 asymmetries
>if only one strong tank
    >no calibration -> break
>define strongest tank as reference
>start minimization
>hand results back to mask()
```

Figure 14: Workflow structure of `calibrate()`. The top section only applies to the asymmetry averaging and is not realized in the charge averaging version.

minimization is applied to the result of this function. `chi()` will be handed a set of asymmetries and then start a loop over this set. For each element, the σ_{ij}-formula and the χ^2-formula from section 3.1 will be computed. The parameters c_i and c_j are chosen by the minimizer based on the result of the χ^2 contribution of each pair (compare with equation 7). To determine the best set of c_i, the contribution of all elements in the `chi()`-loop is added up, which forms the result that is set to be minimized. After the completion of the minimizer, the recovered efficiencies are handed outward to `main()` and the calibration workflow is successfully completed.

4 Data evaluation

In the following, the results of the charge averaging and asymmetry averaging approach will be presented and discussed. Both for the case of proton-showers and γ-showers in the upper and lower chamber separately, leading to four sets of results per approach. Each set was computed from Monte Carlo files containing $\approx 3.6 \times 10^6$ simulated gamma events or, in case of proton simulations, $\approx 4.5 \times 10^6$ events. After applying cuts, the number of considered events is substantially reduced. The full set of generated plots will only be shown here for the upper chamber of proton simulations using the charge averaging approach. All plots of every calibration set can be found in section A.2. The quality of the recovered efficiency parameters c_i is determined by the residual factors R_i. This factor is computed as the difference between c_i and the primary assigned dummy efficiencies g_i.

$$R_i = c_i - g_i \tag{16}$$

Since the residuals define an offset, in the following the will additionally be addressed in such in the following. The results of the charge averaging were found to recover with a significantly higher accuracy. Hence, they will be presented first, and the results of the asymmetry averaging will be discussed afterwards. All percentage values resulting from the calibration are rounded to whole numbers.

4.1 Charge averaging

4.1.1 Proton results

In the following, each set of simulations will be discussed, and the most important result data will be collected in Table 3.

Upper chamber

In Figure 15, the residual offsets resulting from the calibration of a total of 14444 events are displayed. The histogram contains the results of center, middle and belt stage all together. The average residual offset across all stages lies at 15%, with 23% contained within 5% offset. The standard deviation lies at 21%, implying a fair recovery quality for the given amount of statistic. The average offset within each stage varies with the uniformity of the grid illumination, yet only varies in the order of a few percent. Within the 50%, the offsets are spread almost symmetrically around the zero offset, with a small tendency towards positive offsets, and a long tail towards high negative

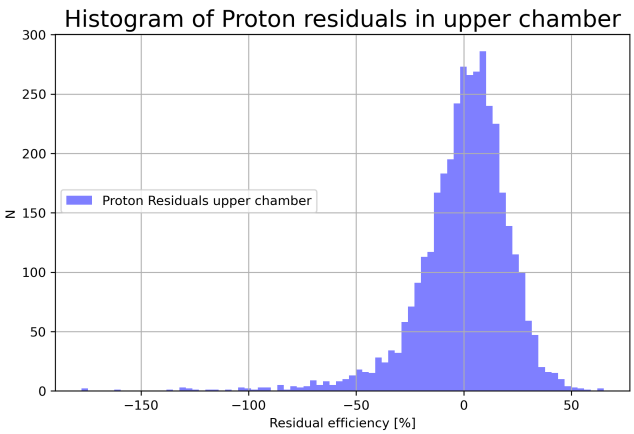

Figure 15: Histogram of the residual offsets in the upper chamber for proton simulations using the charge approach

offsets is explained by dominant charge peaks in the grid. In Figure 16, the residual efficiencies are plotted on the left side and the averaged charges per tank on the right side. A clear connection between a charge peak and a residual peak is observed.

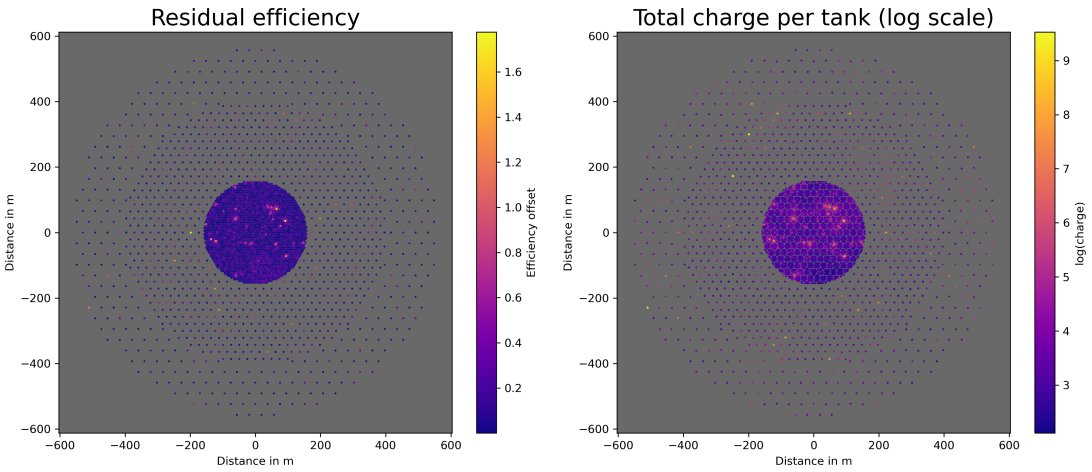

Figure 16: Comparison of the asymmetry assigned to tank i with the averaged charge of all tanks. A connection between asymmetry peaks and charge peaks can be observed.

Lower chamber

The results for investigation in the lower chamber made use of 2233 simulated events and yield an average accuracy of 18% with a contained 19% within 5%. The standard deviation is set at 27%, implying a wider spread of the calibration results. This is explained by the lower amount of statistics available for the lower chamber in the simulation files, since only very high energy events are able to strike the lower chamber. Another effect of this can be found in the increased width of the spread of residuals, which are reaching up to 200% offset when compared to the maximum of around 170% in the upper chamber. The correlation between tank charge and residual offset behaves similar to the upper chamber and can be retraced in Figure 23 displayed in section A.2.1.

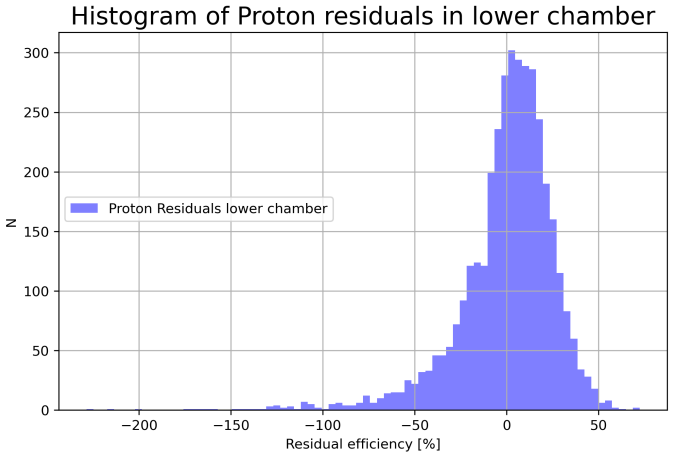

Figure 17: Histogram of the residual offsets in the lower chamber for proton simulations using the charge approach

4.1.2 Gamma results

The results for the γ-simulations are comparable to the proton simulations but lack a few percent of accuracy both on average and for each stage. The standard deviation shows a notable difference to the proton files with 23% for the upper chamber and 35% for the lower chamber. The discussed figures for the proton results plotted for the gamma simulations can be retraced in section 4.2. These show a similar correlation between residual offset and tank charge, which was expected on the basis of the proton results. All plots are shown in section A.2.1.

Set	Events [N]	Std [%]	Accuracy Q [%]	5% containment [%]
p-upper	14444	21	15	23
p-lower	2233	27	19	19
γ-upper	24112	23	17	20
γ-lower	2484	35	25	14

Table 3: Summary of the most important result data from each simulation set with the charge averaging approach

The Proton simulations were found to recover with an overall better quality, since both the standard deviation and 5% containment are higher compared to γ-simulations. Yet a notable difference in both datasets arises from the significant statistical advantage of the γ-simulations. These contain more eligible events in total, which also increases the quality gap between both shower types, since the used proton statistics were 40% smaller than the γ-statistics. The computation time did not change significantly with the number of eligible simulations but rather with the total number of simulations in the concerned files. The computation time also remained comparable for all calibration runs of different cuts, chambers and shower types.

4.2 Asymmetry averaging

The plots for results regarding the asymmetry averaging approach can be found in section A.2.2.

4.2.1 Proton results

Similar to the charge averaging results, the upper chamber recovers better results for the asymmetry averaging results. From Table 4 it can clearly be seen that the quality is not near a satisfactory quality, with up to 200% average offset in the lower chamber. The standard deviation of 2300% in the upper chamber and 1400% in the lower chamber are in line with the low average accuracy. The low levels of containment within 5% points to a general problem of the scaling and calibration in general. Shown in Figure 18 are the residual efficiencies recovered for the calibration run in the upper chamber for proton simulations. This plot was created for a better analysis of the recovery quality.

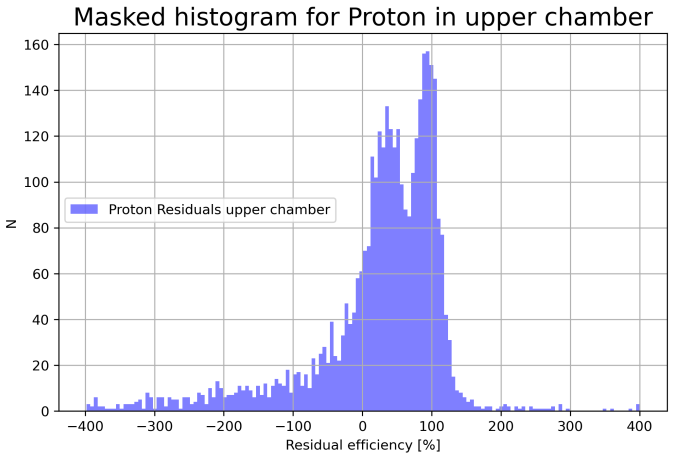

Figure 18: Histogram of the residual offsets in a masked area around the zero offset zone. The offsets are clearly tending towards an offset of 100% rather than 0%.

4.2.2 Gamma results

The gamma results show a little improvement in terms of accuracy and spread for both chambers compared to the proton simulations. In the upper chamber, the average offset is reduced to 170% and a standard deviation of 470%. In the lower chamber, the accuracy yields an average offset of 230% with a standard deviation of 1700%.

Set	Events [N]	Std [%]	Accuracy Q [%]	5% containment [%]
p-upper	14444	2300	200	3
p-lower	2233	1400	160	2
γ-upper	24112	470	170	1
γ-lower	2484	1700	230	1

Table 4: Summary of the most important result data from each simulation set with the asymmetry averaging approach

The conducted calibrations indicate a conceptual problem inherited by the asymmetry averaging approach. Yet the quality of the recovery can be compared within the approach, yielding an advantage for the proton recoveries. The statistics for the upper chamber differ significantly between proton and γ-simulations, which is why a quality comparison is only possible in the lower chamber where statistics are comparable. Here the proton results have a better recovery quality than the γ-results, implying a further recovery advantage of the proton simulations. The accuracy problem is set to arise from the fact that a single WCD unit is incomparable to an IACT telescope since a single WCD tank would rather correspond to a pixel of an IACT telescope camera. When the core location of detected showers varies over multiple events, the asymmetries also fluctuate and will average in the middle, which will, in most cases, be zero. This would then lead to trivial calibrations for a tank pair and efficiencies with a zero value. This exact result is found in the shown histograms and explains the residual peak around 100% offset, that would be the assumed offset in case of a recovered efficiency of 0%.

4.3 Anomaly testing

The anomaly test was only conducted for the charge averaging approach in the upper chamber using proton simulations. This calibration set had the best recovery quality and was therefore chosen to examine possible accuracy losses due to the designed anomaly. They serve the purpose to analyze the change in calibration quality after a possible anisotropy of power supply or total power supply failure for single tanks. For this purpose a *Gradient test* and a *Deactivation test* will be performed. The gradient test is set to simulate a scenario where either an unstable power supply has PMTs run on too high/low voltage, hence affecting the readout efficiency. This test is not fully in line with a realistic scenario, since the individual power supply of each PMT is independent in the tanks, yet it is an intuitive illustration of problems that may influence the quality of the recovery. The choice for a global gradient rather than a gradient within small clusters was made, since for the outer stages the final power supply clusters are still under discussion. Also, it was decided that the asymmetry evaluation in a close proximity around each tank also can be viewed as a simplified cluster environment for this purpose. The deactivation test aims to simulate both the loss of a tank due to PMT failure, significant drop of water levels in the chamber, or just inaccessibility due to maintenance inactivity. For this case tests will be run for different percentages of the grid being deactivated to test the calibration method further.

4.3.1 Deactivation test

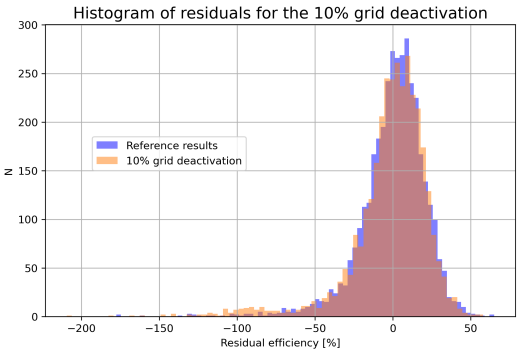

Figure 19: Histogram comparing the results for a 10% deactivation to the regular results.

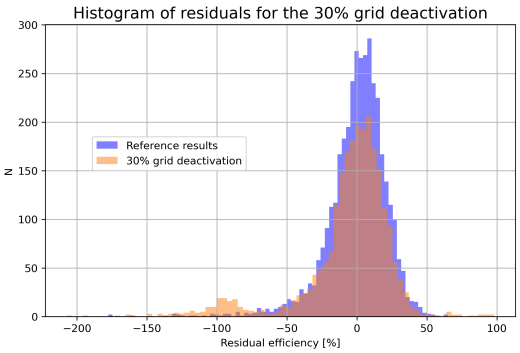

Figure 20: Histogram comparing the results for a 30 % deactivation to the regular results.

The response to grid deactivation was conducted with 10%, 30% and 50% of the grid deactivated. The results for 10% and 30% are shown in Figure 19 and 20, while the histogram of the 50% result is shown in Figure 39 in section A.2.3. For all three cases the recoveries show accuracy levels in agreement with the regular calibration. The peak of the histogram remains centered around 0% offset, with a small peak formed around -100% offset. This peak may be explained by tanks with only a few eligible asymmetries due to the deactivation. Paired with the possibility of a local lack of statistics in a grid region, may result in this kind of precision loss. The side peak increases in significance with the percentage of deactivated tanks, as visible in Figure 20. For the 50% test, this peak cannot be isolated due to a general precision loss. Table 5 summarizes the main quality parameters for each test, as well as the reference calibration. Also Figure 37, 38 and 40 show the effects of the deactivation of the residuals in the grid. For increasing percentage of deactivation the former correlation of charge peaks and residual peaks is lost and dominated by low calibration capability for individual tanks.

Set	Number of events	Std [%]	Total accuracy Q [%]	5% containment [%]
Reference	14444	21	15	23
10%	7285	26	17	20
10%	14444	25	17	20
30%	7285	33	21	14
30%	14444	33	21	13
50%	14444	56	45	3

Table 5: Results for 10% and 30% grid deactivation. Both tests were run for different statistics to highlight the gain of accuracy with significantly higher statistics.

The included test regarding the effect of considered statistics for 10% and 30% deactivation shows no significant effect of statistics-dependent accuracy within the scope of this work.

4.3.2 Gradient test

For this test an additional efficiency factor is added to the grid so that the right end of the grid has a $X\%$ higher efficiency than the left end. The calibration was tested for a moderate gradient of 10% and also for more severe effects with a 30% gradient. Shown in Figure 21 is the reference histogram of the regular calibration run now including the results for a 10% gradient.

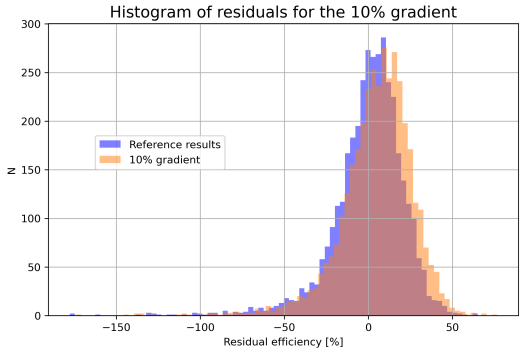

Figure 21: Histogram comparing the results for a 10% gradient to the regular results.

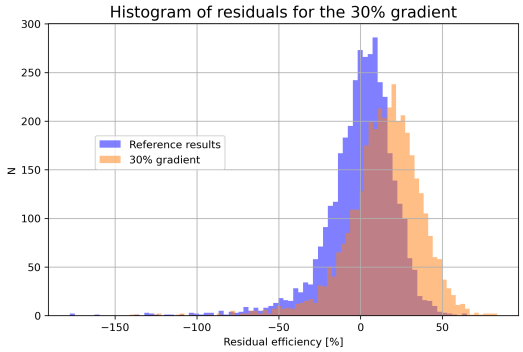

Figure 22: Histogram comparing the results for a 30 % gradient to the regular results.

For the 10% gradient the average accuracy of the recovered efficiencies is comparable to the regular calibration results. Yet the peak of the histogram is shifted further in the direction of positive offsets. This effect is clearer for the 30% offset and indicates a systematical effect of the gradient. The overall offset of the entire histogram and therefore a precision loss is clearly linked to the slope of the efficiency gradient. Yet comparison of the results found with less statistics indicates that an increase of statistics might resolve this problem. Table 6 summarizes the main quality parameters for each test as well as the reference calibration. The resolving power of a doubled amount of statistics is found to be small, yet notable within the scope of this work.

Set	Number of events	Std [%]	Total accuracy Q [%]	5% containment [%]
Reference	14444	21	15	23
10%	7285	22	17	18
10%	14444	22	17	19
30%	7285	23	23	11
30%	14444	22	22	13

Table 6: Results for 10% gradient and 30% gradient. Both tests run for different statistics to highlight the gain of accuracy with significantly higher statistics.

5 Conclusion and outlook

In this thesis, the approach of cross-calibration was discussed for the possible application on ground-based water Cherenkov detectors. The calibration was done for Monte Carlo simulations of proton and γ-induced air showers. An original approach of CTA was adapted to test the efficiency calibration by utilizing charge asymmetry parameters to calibrate the effective efficiencies of the WCD grid. An approach in line with established usability for IACTs, which uses asymmetry parameters averaged over multiple events, suffered from structural problems preventing accurate calibrations in case of a WCD application. A second approach specifically designed for WCDs has proven to be effective. The new approach uses averaged tank charges, which were then used to compute asymmetries. The results of the conducted calibrations have shown satisfactory accuracy within the scope of the considered statistics. Comparison between proton and γ-statistics has shown that the calibration is more effective for proton events, which is a result of the weighted asymmetry computation favoring the lateral intensity pattern of proton showers over a uniform γ-shower pattern. It is yet to be noted that from the response to simulation data no final statement of the behavior with real shower data can be made. The intensity pattern of a real shower still differs from simulations and for that reason a real favoring of an event type can not be stated. In addition to feasibility tests, a set of anomalies that might interfere with the recovery quality have been tested. The results have shown satisfactory response of the charge averaging approach to conducted tests with an added efficiency gradient and a set of partial grid deactivation.

All this leads to the conclusion that the cross-calibration technique has proven to be successful in recovering efficiency parameters for ground-based water Cherenkov detectors like the SWGO. By increasing statistics and ensuring a more uniform illumination throughout the grid, the negative effects of local charge peaks may be resolved. This will lead to overall lower residuals and therefore improve the recovery accuracy.
Further possible optimizations mainly concern the briefly introduced ring averaging approach which was formed as a constraining approach of the original CTA idea. This approach may resolve the averaging problem discussed for the asymmetry averaging approach conducted here. Yet it needs to be addressed that this approach relies on a lateral intensity pattern that allows the definition of a ring system around the shower core. This investigation may require a significant amount of real shower data to ensure that the ring structure is formed in a constructive manner. Further, a test of this approach by the use of simulation data similar to the data here may be questionable because these simulations have already been questioned for their accuracy. The optimization of an approach around Monte Carlo simulations might be misleading for that fact.
Optimizations of the charge averaging approach would concern technical details to further reduce computation time and improve the response to an amount of statistics which would allow for a precise calibration. For the amount of statistics used during this thesis the current structure of implementation may work effectively, but an increase of events by a few orders would severely impact the time needed to qualify all events.

Taken together, the work of this thesis provides a foundation for a robust cross-calibration pipeline that can be tested with real data and then used to monitor SWGO-like WCD efficiencies.

A Appendix

A.1 Regarding the implementation

A.1.1 Simulation file structure

```
fields = [
    "mc.logEnergy", #0
    "mc.Xmax", #1
    "mc.zenithAngle", #2
    "mc.azimuthAngle", #3
    "mc.coreX", #4 center impact
    "mc.coreY", #5 center impact
    "mc.corsikaParticleId", #6 14=proton, 1=gamma
    "event.hit.charge", #7 voltage from pmt proportional to photons
    "event.hit.time", #8 time of detection per tank
    "event.nHit", #9 number of hits
    "event.hit.xPMT", #10 x position of PMT in m
    "event.hit.yPMT", #11 y position of PMT in m
    "event.hit.zPMT", #12 z position of PMT in m
    "event.hit.gridId", #13 identifies if hit was in upper or lower tank
    "event.hit.tankId", #14 identifies if hit was in upper or lower tank
    "rec.LHLatDistFitEnergy", #15
    "mc.delCore", #16 quality of reconstructed core position
    "mc.delAngle", #17 quality of reconstructed angle
    "mc.coreR", #18 quality of reconstructed core radius
    "rec.LHLatDistFitMinLikelihood", #19
    "planeFit2.chiSq", #20
    "planeFit2.Ndof", #21
    "planeFit2.theta", #22
] # load only the fields from the root file that are useful for you
```

A set of CORSIKA simulation fields containing simulation data of an event. Not all fields on display have been used for this work and the comments were added for convenience.

A.2 Regarding the calibration results

A.2.1 Regarding the charge averaging approach

Lower chamber proton results

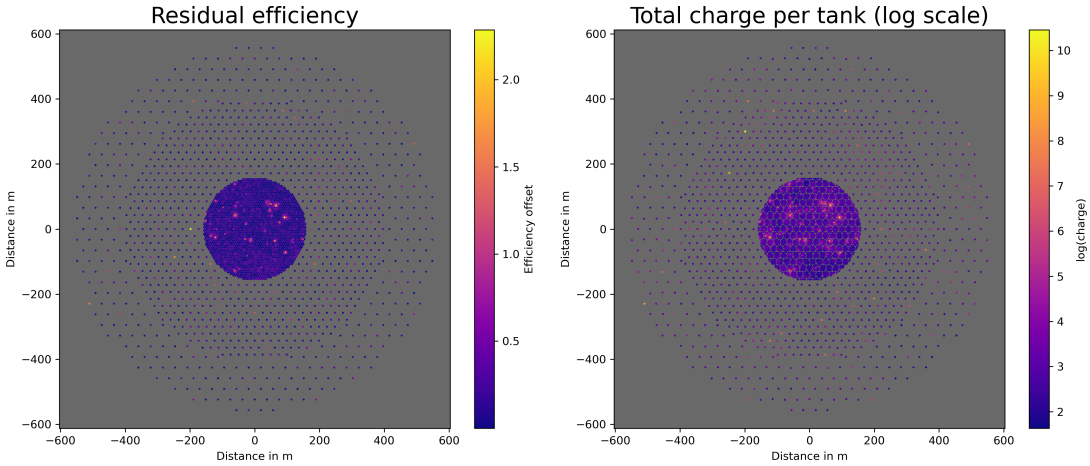

Figure 23: Correlation between residual offsets and charge per tank shows similar behavior as in the lower chamber

Upper chamber γ-results

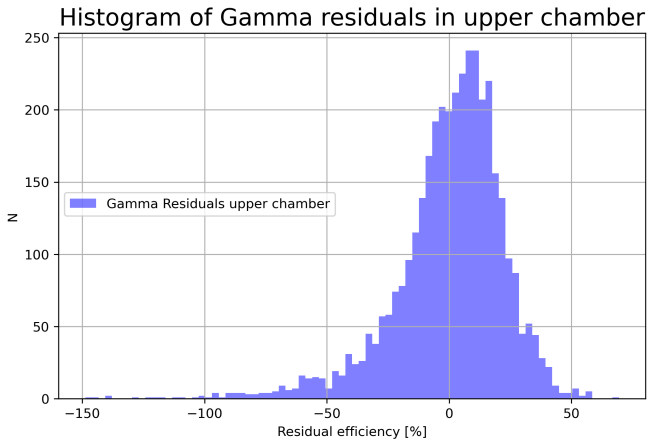

Figure 24: Histogram of the distribution of residual offsets for γ-simulations in the upper chamber.

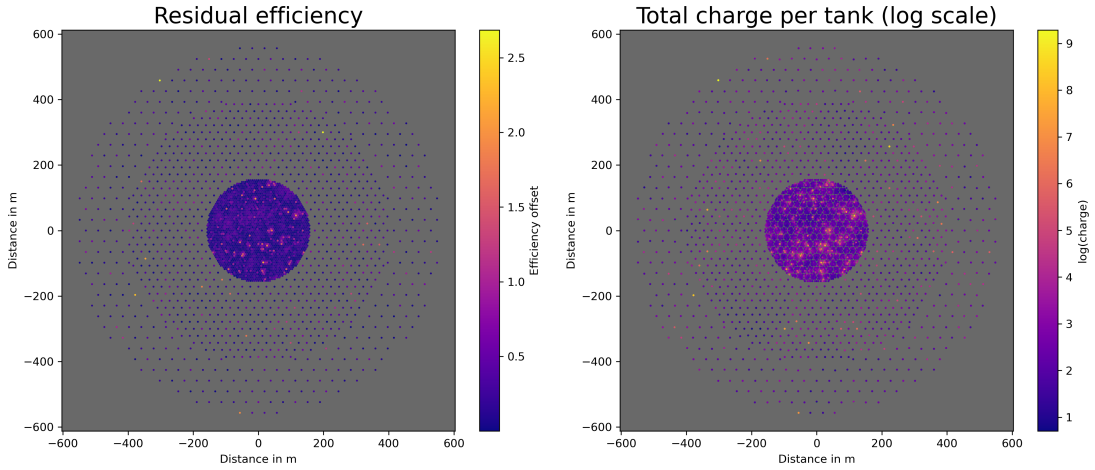

Figure 25: Correlation between residual offsets and charge per tank shows similar behavior as in the lower chamber

Lower chamber γ-results

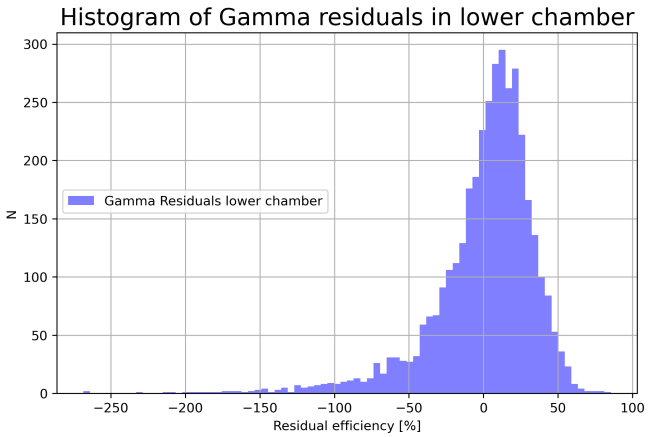

Figure 26: Histogram of the distribution of residual offsets for γ-simulations in the lower chamber.

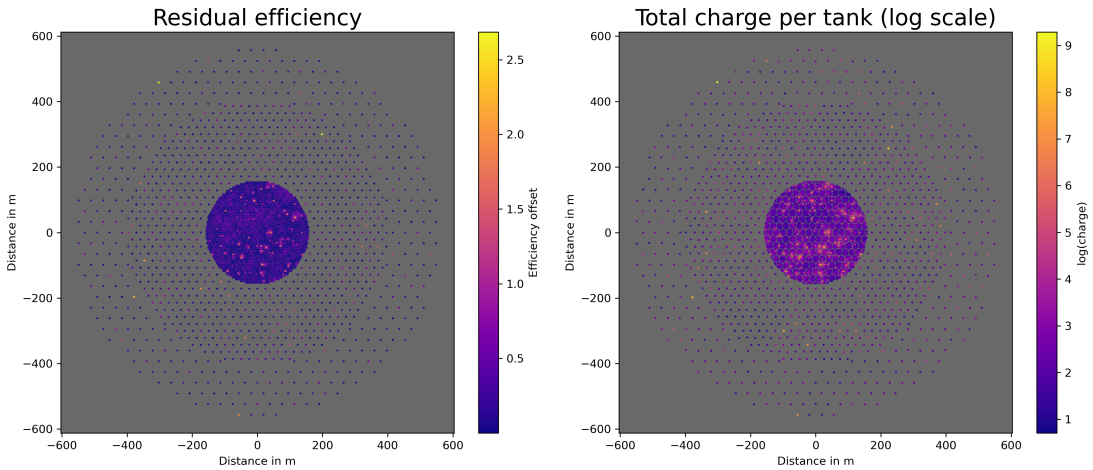

Figure 27: Correlation between residual offsets and charge per tank shows similar behavior as in the lower chamber

A.2.2 Regarding the asymmetry averaging approach

Lower chamber proton results

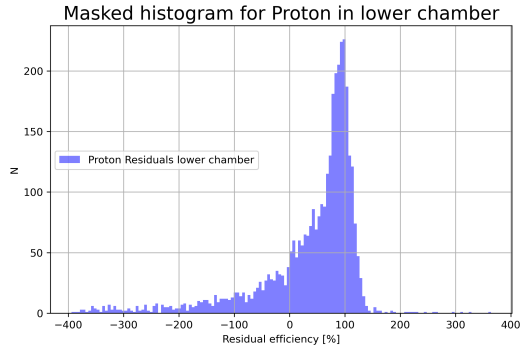

Figure 28: Masked histogram to show only the proximity around the zero residual offset

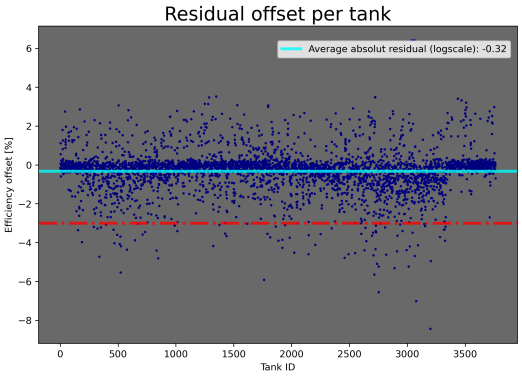

Figure 29: Residuals in log scale

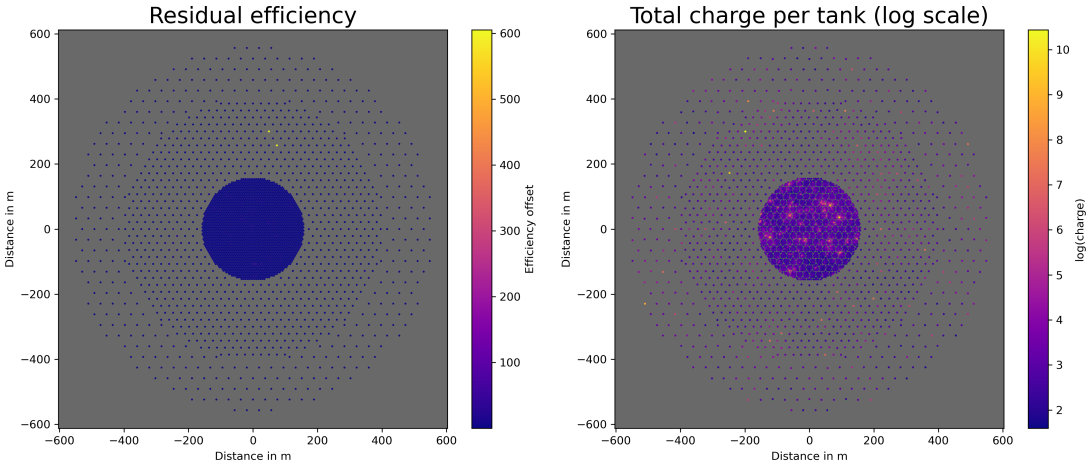

Figure 30: Comparison of residual offsets with the averaged charge per tank for the lower chamber

Upper chamber γ-results

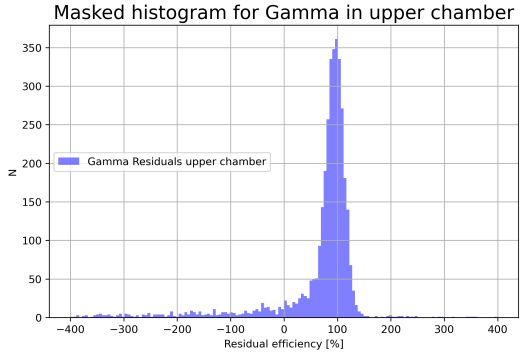

Figure 31: Masked histogram to show only the proximity around the zero residual offset

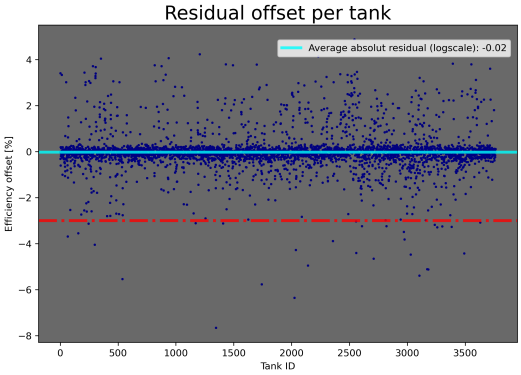

Figure 32: Residuals in log scale

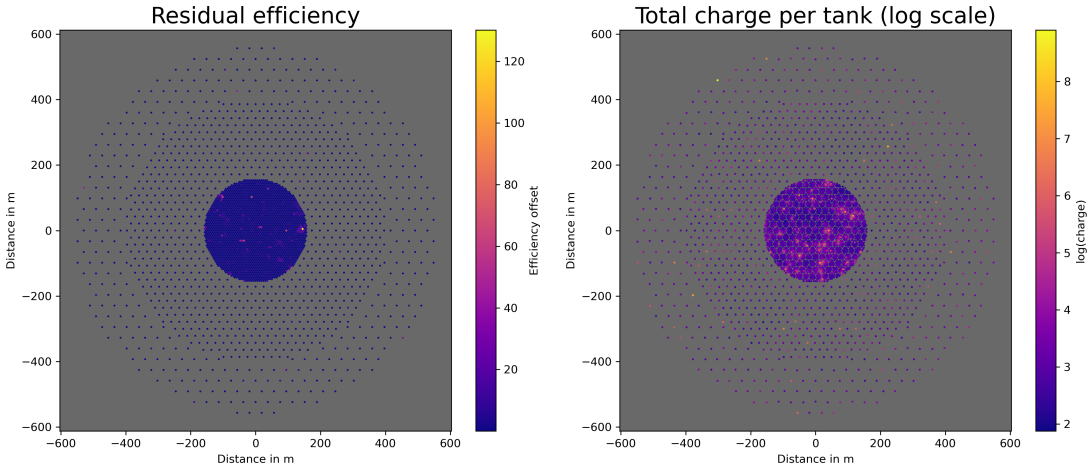

Figure 33: Comparison of residual offsets with the averaged charge per tank for the upper chamber

Lower chamber γ-results

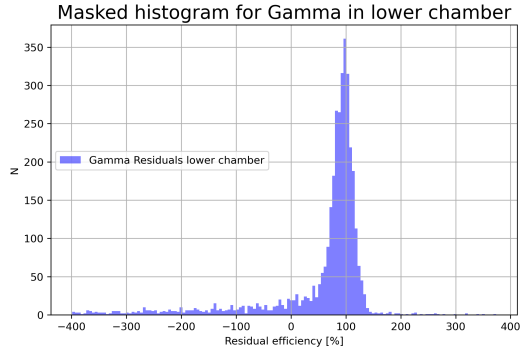

Figure 34: Masked histogram to show only the proximity around the zero residual offset

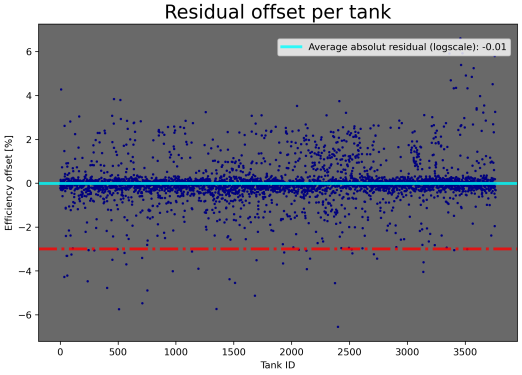

Figure 35: Residuals in log scale

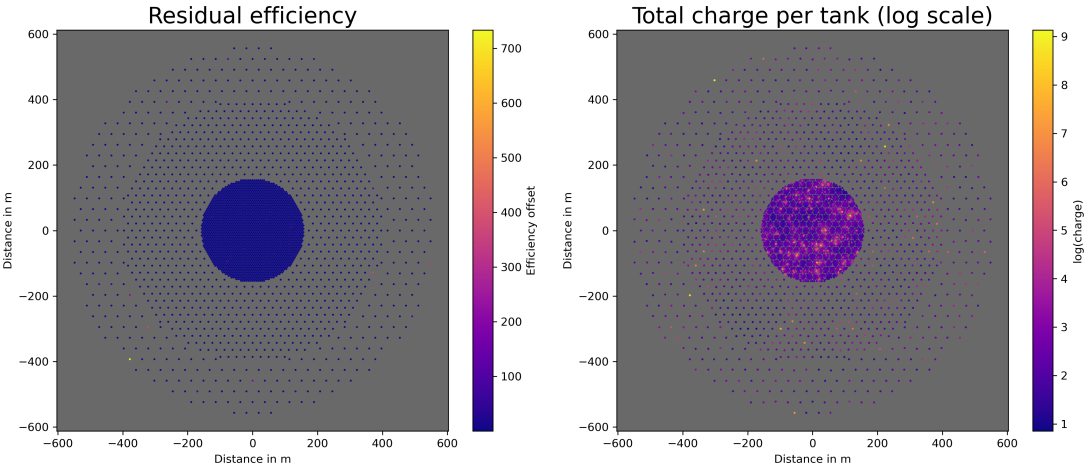

Figure 36: Comparison of residual offsets with the averaged charge per tank for the lower chamber

A.2.3 Regarding the Anomaly testing

10% Deactivation test

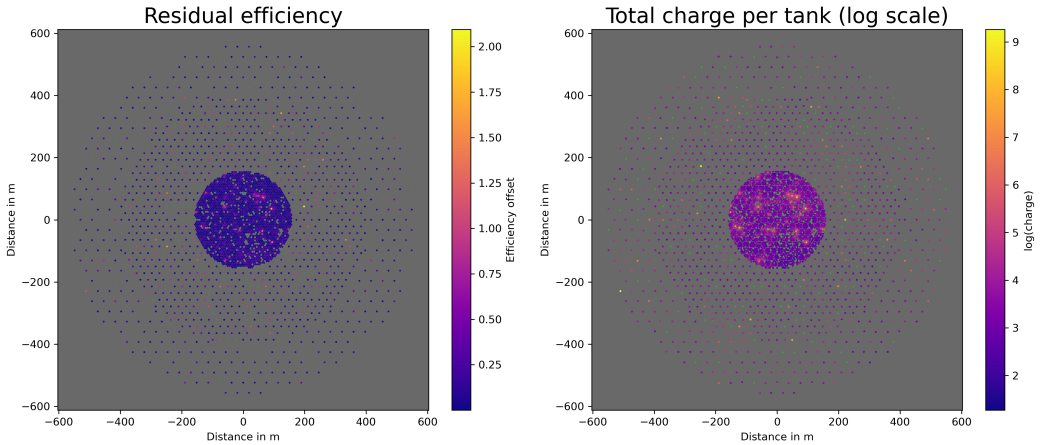

Figure 37: Grid with 10% deactivated tanks. The plots show strong correlation between residual offset and charge peak in a tank.

30% Deactivation test

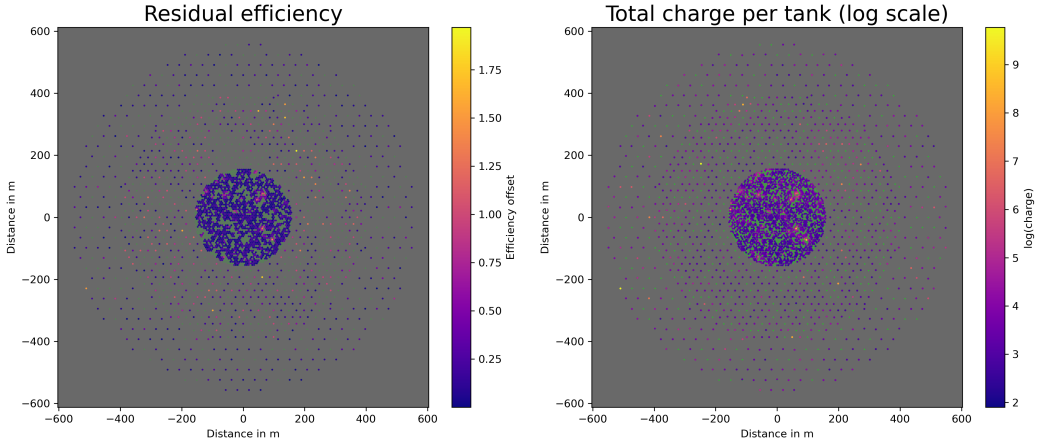

Figure 38: Grid with 30% deactivated tanks. The plots still show correlation between residual offset and charge peak in a tank yet accuracy losses for tanks without charge peaks can be found.

50% Deactivation test

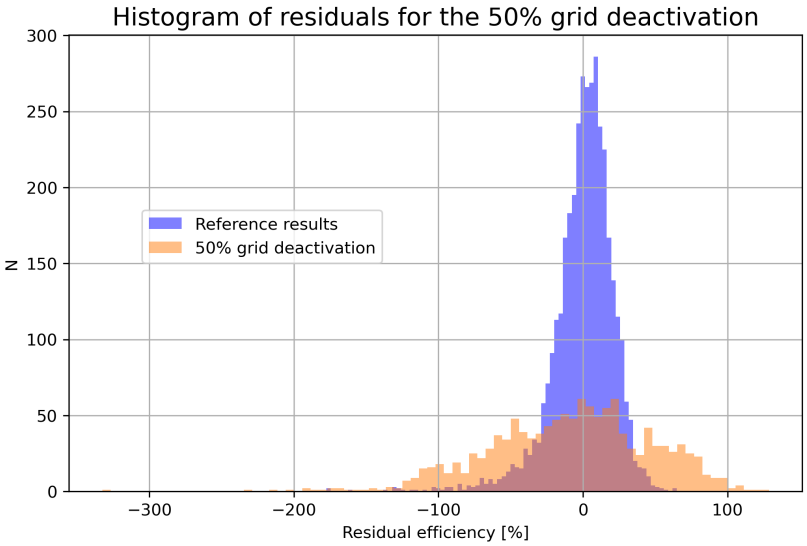

Figure 39: Histogram comparing the regular results to those with 50% of the grid being deactivated

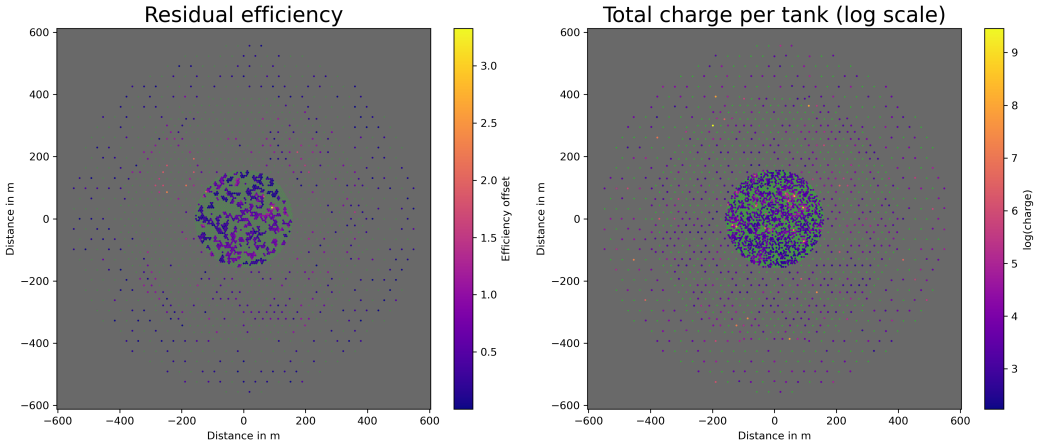

Figure 40: Grid with 50% deactivated tanks. The plot shows that the correlation of high residuals and charge peaks is lost and residuals are dominated by poor comparability to neighboring tanks.

Bibliography

Abeysekara, A. U., A. Albert, R. Alfaro, C. Alvarez, et al. (June 2017). "Observation of the Crab Nebula with the HAWC Gamma-Ray Observatory". In: *The Astrophysical Journal* 843.1, p. 39. ISSN: 1538-4357. DOI: 10.3847/1538-4357/aa7555. URL: http://dx.doi.org/10.3847/1538-4357/aa7555.

Abreu, Pedro, Andrea Albert, Ruben Jose Alfaro, Alexander Alfonso, et al. (2023). *Status of the SWGO air shower reconstruction using a template-based likelihood method*. DOI: 10.22323/1.444.0593.

D. Heck J. Knapp, J.N. Capdevielle G. Schatz T. Thouw (1998). "CORSIKA: A Monte Carlo Code to Simulate Extensive Air Showers". In.

DESY, Deutsches Elektronen-Synchrotron (2025a). *CORSIKA Shower Images: Photon Shower*. https://www-zeuthen.desy.de/~jknapp/fs/photon-showers.html. [Online; accessed 10-December-2025].

— (2025b). *CORSIKA Shower Images: Proton Shower*. https://www-zeuthen.desy.de/~jknapp/fs/proton-showers.html. [Online; accessed 10-December-2025].

Foith, Florian (2025). https://git.ecap.work/ow48efub/swgo_cross-calibration. Repository containing the used implementation of this work.

HAWC, The High-Altitude Water Cherenkov Gamma-Ray Observatory (2025). *The HAWC Collaboration*. https://www.hawc-observatory.org/collaboration/. [Online; accessed 14-December-2025].

Hofmann, Werner (Oct. 2003). "Intercalibration of Cherenkov telescopes in telescope arrays". In: *Astroparticle Physics* 20.1, 1–3. ISSN: 0927-6505. DOI: 10.1016/s0927-6505(03)00137-3. URL: http://dx.doi.org/10.1016/S0927-6505(03)00137-3.

Kunwar, Samridha, Hazal Goksu, Jim Hinton, Harm Schoorlemmer, et al. (2023). "A double-layered Water Cherenkov Detector array for Gamma-ray astronomy". In: *Nuclear Instruments and Methods in Physics Research Section A: Accelerators, Spectrometers, Detectors and Associated Equipment* 1050, p. 168138. ISSN: 0168-9002. DOI: https://doi.org/10.1016/j.nima.2023.168138. URL: https://www.sciencedirect.com/science/article/pii/S0168900223001286.

Matthews, J. (2005). "A Heitler model of extensive air showers". In: *Astroparticle Physics* 22.5-6, pp. 387–397. ISSN: 0927-6505. DOI: 10.1016/j.astropartphys.2004.09.003. URL: https://www.sciencedirect.com/science/article/pii/S0927650504001598 (visited on 11/16/2025).

Mitchell, A.M.W., R.D. Parsons, W. Hofmann, and K. Bernlöhr (Feb. 2016). "Cross calibration of telescope optical throughput efficiencies using reconstructed shower energies for the Cherenkov Telescope Array". In: *Astroparticle Physics* 75, 1–7. ISSN: 0927-6505. DOI: 10.1016/j.astropartphys.2015.10.008. URL: https://www.sciencedirect.com/science/article/pii/S0927650515001486?via%3Dihub.

Sinnis, Gus (2010). "Water Cherenkov technology in gamma-ray astrophysics". In: *Nuclear Instruments and Methods in Physics Research Section A: Accelerators, Spectrometers, Detectors and Associated Equipment* 623.1. 1st International Con-

ference on Technology and Instrumentation in Particle Physics, pp. 410–412. ISSN: 0168-9002. DOI: https://doi.org/10.1016/j.nima.2010.03.019. URL: https://www.sciencedirect.com/science/article/pii/S0168900210005838.

SWGO-Collaboration, P. Abreu, R. Alfaro, A. Alfonso, et al. (2025). *Science Prospects for the Southern Wide-field Gamma-ray Observatory: SWGO*. arXiv: 2506.01786 [astro-ph.HE]. URL: https://arxiv.org/abs/2506.01786.

Acknowledgements

- Thanks to Martin Schneider and Dr. Alison Mitchell for their support with technical and subject specific questions.
- Thanks to the participants of the SWGO ASWG call on December 5, 2025 for their comments on my work, especially regarding the alternative asymmetry averaging approach and its difficulties.

Declaration of Originality

I, Florian Foith, student registration number: 23113482, hereby confirm that I completed the submitted work independently and without the unauthorized assistance of third parties and without the use of undisclosed and, in particular, unauthorized aids. This work has not been previously submitted in its current form or in a similar form to any other examination authorities and has not been accepted as part of an examination by any other examination authority.

Where the wording has been taken from other people's work or ideas, this has been properly acknowledged and referenced. This also applies to drawings, sketches, diagrams and sources from the Internet.

In particular, I am aware that the use of artificial intelligence is forbidden unless its use an aid has been expressly permitted by the examiner. This applies in particular to chatbots (especially ChatGPT) and such programs in general that can complete the tasks of the examination or parts thereof on my behalf.

Any infringements of the above rules constitute fraud or attempted fraud and shall lead to the examination being graded "fail" ("nicht bestanden").

Place, Date	Signature